Research paper

Macro-indentation testing of soft biological materials and assessment of hyper-elastic material models from inverse finite element analysis

Venkat Ayyalasomayajula [a,*], Øyvind Ervik [b,c], Hanne Sorger [b,c], Bjørn Skallerud [a]

[a] *Department of Structural Engineering, Norwegian University of Science and Technology, Trondheim, 7052, Norway*
[b] *Department of Circulation and Medical Imaging, Norwegian University of Science and Technology, Trondheim, 7052, Norway*
[c] *Clinic of medicine, Nord-Trøndelag Hospital Trust, Levanger Hospital, Levanger, 7600, Norway*

ARTICLE INFO

ABSTRACT

Mechanical characterization of hydrogels and ultra-soft tissues is a challenging task both from an experimental and material parameter estimation perspective because they are much softer than many biological materials, ceramics, or polymers. The elastic modulus of such materials is within the 1 - 100 kPa range, behaving as a hyperelastic solid with strain hardening capability at large strains. In the current study, indentation experiments have been performed on agarose hydrogels, bovine liver, and bovine lymph node specimens. This work reports on the reliable determination of the elastic modulus by indentation experiments carried out at the macro-scale (mm) using a spherical indenter. However, parameter identification of the hyperelastic material properties usually requires an inverse finite element analysis due to the lack of an analytical contact model of the indentation test. Hence a comprehensive study on the spherical indentation of hyperelastic soft materials is carried out through robust computational analysis. Neo-Hookean and first-order Ogden hyperelastic material models were found to be most suitable. A case study on known anisotropic hyperelastic material showed the inability of the inverse finite element method to uniquely identify the whole material parameter set.

1. Introduction

Accurate modeling of biological tissue is important for numerical simulations of clinical treatments. High-fidelity models are required in surgical simulators to accurately simulate realistic tool-tissue interactions incorporating haptic feedback and soft tissue deformation during surgery. In this regard, knowledge of the mechanical properties of ultra-soft tissues is of particular interest as they are highly susceptible to various diseases including cancers, which in turn may lead to altered mechanical properties (Huang et al., 2014; Masuzaki et al., 2007; Tourasse et al., 2012). Such a characterization relies on experimental data with well-defined kinematic and kinetic boundary conditions, such that an analytical formulation or an inverse problem could be solved.

The diagnosis of cancer involves a series of medical procedure and test to determine the presence, nature, location, and extent of the cancer. A biopsy is typically the most definitive diagnostic method for cancers (Postmus et al., 2017; Vilmann et al., 2015). Diagnostic imaging techniques such as ultrasound shear wave elastography (USSWE) (Barr, 2018; Ferraioli et al., 2014) and magnetic resonance elastography (MRE) (Venkatesh et al., 2013; Hoodeshenas et al., 2018) can be used to identify qualitatively the elasticity values of soft tissues in vivo in the presence of fibrosis and cancers. However, qualitative

methods can be limiting in their interpretability and cancer diagnosis compared to quantitative elastography. Further, they are prone to inter-examiner variability. In, contrast, quantitative shear wave ultrasound provides numerical values for tissue stiffness by measuring the speed of shear waves propagating through tissue, offering stiffness values in units like kilopascals (kPa) (Bercoff et al., 2004). Compared with MR elastography, ultrasound methods are fast to perform and relatively inexpensive (Oudry et al., 2009). Ultrasound-based methods have limited depth penetration and restricted field of view, which can make it challenging to visualize organs located deep within the body. This often requires the operator to scan and adjust the probe position to fully visualize the entire organ (Franchi-Abella et al., 2013). Alternatively, minimally invasive indentation techniques impose deformation on tissue locally using probes equipped with tactile sensors to measure the force–displacement response (Abushagur et al., 2014; Han et al., 2003). However, the above-mentioned techniques require rigorous validation, which is often done by ex-vivo mechanical testing.

Metastases to the lymphatic system are common in most cancers (Das and Skobe, 2008). Cervical lymph nodes are common sites of metastatic involvement from primary cancers of the head and neck,

---

breast, and lung. Moreover, malignant lymphomas and leukemias frequently involve cervical lymph nodes (Baatenburg de Jong et al., 1989). Moreover, in the head and neck region, malignant lymphoma is also common in cervical lymph nodes (DePeña et al., 1990). Information on the stiffness of lymph nodes in any species is limited. However, to date, there are only a couple of studies that reported the stiffness of resected lymph nodes (Miyaji et al., 1997; Yuen et al., 2011). On the other hand, agarose hydrogels (Markert et al., 2013; Hamhaber et al., 2003) and liver tissues (Kiss et al., 2009; Mazza et al., 2007; Mattei and Ahluwalia, 2016) have been tested ex-vivo extensively. In order to measure the quantitative responses of soft tissues ex-vivo, numerous techniques including compression and tension (Brunon et al., 2010; Chui et al., 2004; Hu and Desai, 2004), indentation (Chai et al., 2013; Yang et al., 2020), and aspiration (Mazza et al., 2007; Nava et al., 2008) have been proposed. In vivo soft tissue deformation, the tissue is subject to compression, tension, and shear. When liver tissue is subject to different forms of deformation, it shows different mechanical characteristics (Gao et al., 2010). Soft tissue indentation is affected by both the compressive and tensile characteristics of the tissue and proves to be a promising tool for mechanical characterization. To date, however, it remains a challenging issue to measure the hyperelastic properties of soft materials in a local area or at small scales. Using commercial spherical indenters, indentation tests can be easily performed across different length scales.

In recent years, measuring the mechanical properties of hyperelastic materials using indentation tests has attracted considerable attention. For example, Lee et al. (2003) developed a spherical indentation approach to evaluate the material properties of rubber materials described by the Yeoh model. Samani and Plewes (2004) proposed an inverse method to interpret the nonlinear indentation force–displacement response to derive the hyperelastic parameters of small ex vivo tissue samples. Giannakopoulos and Triantafyllou (2007) addressed the spherical indentation of incompressible rubbery materials through theoretical and experimental efforts. Their theoretical analysis based on the Mooney–Rivlin model led to an analytical solution for the indentation load–depth curve with the ratio of the indentation depth to the indenter radius smaller than 10%. Chen et al. (2021) characterized non-linear viscoelastic material data from indentation test data. Lin et al. (2009) proposed load–depth relations for several hyperelastic strain energy functions and validated the solutions for the ratio of the indentation depth to the indenter radius smaller than 20% via finite element simulations. However, several issues remain, which deserve further effort.

The force–displacement response of ultra-soft tissues from indentation tests is often non-linear (Holzapfel et al., 2001). For very small deformation levels, an equivalent elastic modulus can be computed from known analytical solutions (Shuman et al., 2006; Hay, 2009). However, an analytical solution does not exist for a similar computation of hyperelastic material parameters as aforementioned. Inverse finite element (FE) modeling offers a fast and accurate way of determining hyperelastic material properties from indentation test data (Sangpradit et al., 2011; Zisis et al., 2015). For instance, Feng et al. demonstrated the characterization of brain white matter with transversely isotropic via inverse FE analysis using multiple rectangular indentation configurations (Feng et al., 2017). The uniqueness of the identified parameter set for a model with more than two unknowns is conditional (Pan et al., 2016; Namani and Simha, 2009). Nonetheless, an analysis of commonly employed hyperelastic models and their material parameter identification from indentation test data for agarose hydrogel phantoms liver tissue, and lymph nodes is not available.

Agarose phantoms and liver tissues are commonly employed in benchmarking studies while evaluating shear wave elastography, prior to testing on cervical lymph nodes. The knowledge of their elastic modulus is therefore fundamental to the success of such studies. The objective of the paper is twofold: firstly to demonstrate the reliability of macro-indentation in determining the elastic modulus of agarose

hydrogels and bovine soft tissue specimens (liver and lymph nodes) at the mm length scale. In particular, the analysis of lymph node elasticity is an integral part of a project on USSWE for the detection of lung cancer. The comparison of elasticity measurements from USSWE will be presented in an accompanying study. Secondly, a detailed inverse FE analysis to identify the local hyperelastic material properties is presented. The results from Hertzian elastic contact solutions and finite element modeling accounting for hyperelasticity are discussed and compared.

2. Methods

2.1. Material and sample preparation

Hydrogel phantoms were made from plant-based agar (Type I-A, low EEO, Agarose A0169, Sigma-Aldrich) that was mixed with water and condensed milk, heated on a Corning PC-420D hotplate (Corning, NY) until the liquid reached the target temperature, and then cooled to form a solid gel (McIlvain et al., 2019). Temperature was measured periodically during the heating process using a standard scientific thermometer; as a result of constant stirring of the liquid, temperature was assumed to be homogeneous throughout. Phantom creation parameters of interest included agar concentration (0.4%, 0.7%, and 1%), hot plate temperature, stir rate, final liquid temperature, whether a lid was used during heating, and cooling rate determined by cooling location. The prepared phantoms were cut into cuboids of size 2.5 cm × 2.5 cm × 1.2 cm for indentation testing.

The whole liver of three healthy cows was obtained from a local butchery. For each animal, the tissues were transported to the laboratory within 2 h of it being sacrificed. Five cuboid blocks of tissue were dissected from each liver with dimensions of 2.5 cm × 2.5 cm × 1.2 cm, amounting to a total of 15 samples.

The tissues surrounding the cervical and thoracic region of the cow were investigated for lymph nodes. A total of 8 lymph nodes were resected from the surrounding tissues. The lymph nodes varied in size and, therefore were measured and weighed with a digital caliper and an electronic scale respectively.

Since all the tissues were not tested on the same day, they were transferred to the freezer operating at −28 °C until the day of testing. On the day of testing, the tissue samples were first thawed in a phosphate buffer saline solution (PBS) at 4 °C for 2 h and then at room temperature for another 2 h.

2.2. Macroindentation tests

The experimental setup is shown in Fig. 1a. Indentation was conducted at room temperature (∼24 °C). A custom-made 3-d printed spherical indenter of radius 0.5 mm was used. It was coupled to a 1 N load cell (LSB200, Futek Advanced Sensor Technology Inc., Irvine, CA, USA) and driven by a linear stepper motor with a precision of 0.01 mm (UBL23, Saia-Burgess Inc., OH, USA) which was in turn coupled to a linear variable differential transformer (LVDT) displacement transducer (DC15, Salartron Metrology Ltd., Leicester, UK) by a custom-made device. The entire system was computer-controlled through the user interface of software developed in-house using LabView/CVI 8.5 (National Instruments Co., TX, USA).

The samples were placed on a horizontal platform sprayed with a thin layer of PBS that provided lubrication and prevented them from dehydration. The platform was adjusted vertically so that the starting position of the indenter was slightly above the sample. Indentation tests, each consisting of 3 cycles of loading and unloading, were performed at an indenter speed of approximately 0.05 mm/s. The maximum indentation depth was set to be about 20% of the initial thickness of the slice. For each sample, 5 points were marked prior to testing to create a map of the elasticity.
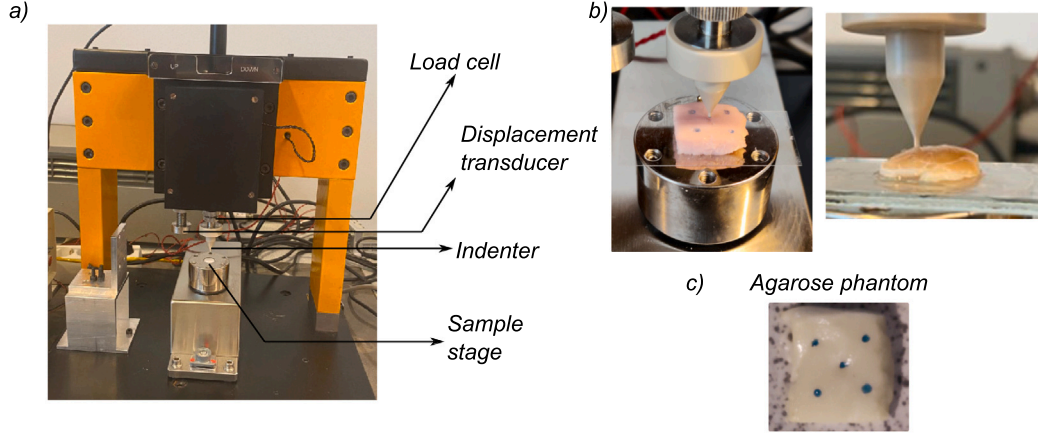
Fig. 1. (a) The indentation test setup used for the experiments; (b) Agarose phantom sample and lymph node sample undergoing indentation testing; (c) a schematic of the points tested per each sample.

The slope of the unloading curve S at the maximum indentation depth data point is used to calculate the elastic modulus by using the following equations.

$$S = \frac{\partial P}{\partial x} \tag{1}$$

from which we compute the quantity E_r:

$$E_r = \frac{\pi}{2} * \frac{S}{\sqrt{A}} \tag{2}$$

where A is the projected area for a given indenter:

$$A = 2\pi R h_c \tag{3}$$

where R is the indenter radius and h_c is effective indentation depth. Finally, the material's elastic modulus can be estimated by:

$$E_{estimate} = E_r[1 - v^2] \tag{4}$$

Assuming the material is nearly incompressible, the elasticity was estimated for a Poisson's ratio value of 0.45. It is established that a 40% uncertainty in Poisson's ratio results in only a 5% uncertainty in the estimated elastic modulus of the sample (Hay, 2009).

2.3. Constitutive models

Ultra-soft biological materials are often considered to be isotropic, hyperelastic, and incompressible (Fung, 2013). The mechanical response of such materials could be described by using a strain–energy function Ψ defined per unit reference volume. In this study, we investigate four hyperelastic models, including neo-Hookean, Mooney–Rivlin, Yeoh, and first-order Ogden hyperelastic, which have been widely applied to model the nonlinear deformation behavior of rubber-like materials and biological soft tissues. These strain energy density functions are briefly introduced as follows.

$$\Psi^{NH} = C_1(I_1 - 3) \quad ; \quad I_1 = \sum_{i=1}^{3} \lambda_i^2 \tag{5}$$

$$\Psi^{MR} = C_1(\tilde{I}_1 - 3) + C_2(\tilde{I}_2 - 3);$$

$$I_1 = \sum_{i=1}^{3} \lambda_i^2 \quad ; \quad I_2 = \lambda_1^2\lambda_2^2 + \lambda_2^2\lambda_3^2 + \lambda_3^2\lambda_1^2; \tag{6}$$

$$\tilde{I}_1 = J^{-2/3} I_1 \quad ; \quad \tilde{I}_2 = J^{-4/3} I_2 \quad ; \quad J = \lambda_1\lambda_2\lambda_3$$

$$\Psi^{YH} = C_1(I_1 - 3) + C_2(I_1 - 3)^2 + C_3(I_1 - 3)^3 \tag{7}$$

$$\Psi^{OG} = \frac{2\mu}{\alpha^2}(\lambda_1^\alpha + \lambda_2^\alpha + \lambda_3^\alpha - 3) \tag{8}$$

where μ is the shear modulus, λ_i are the principle stretches, and C_i, α are material constants. For a comprehensive study of the hyperelastic material theory and derivation of stress–stretch relationships for the above models, the reader is directed to Smith (2010) and Melly et al. (2021).

2.4. Finite element model and inverse analysis

To represent the indentation test setup for the inverse finite element analysis (FEA), a 2-D axisymmetric model was employed for the simulation of the elastic behavior of the material (Smith, 2010). A spherical rigid indenter was used in the axisymmetric model which has the same projected area-to-depth function as the custom-made indenter. The sample was meshed with four-node bilinear axisymmetric quadrilaterals, and reduced integration elements (CAX8RH), as shown in Fig. 2a. A fine mesh was used under the contact area and near the tip of the indenter to study the stress distribution under the indenter more accurately. In order to reduce the computational time, a coarser mesh was used further away from the indenter tip. The non-linear geometry option was used in the finite element simulation.

Both the loading and unloading steps of the indentation process were simulated in the finite element model. During the loading stage, the indenter was driven into the specimen surface in the axial direction up to 20% of its thickness and with a constant speed. This provides the loading part of the load–displacement curve in the finite element simulation. When the indenter tip reached the preset maximum penetration depth, the test specimen was unloaded and the indenter tip returned to its initial position with the same speed as that of the loading stage. The boundary conditions were applied along the center line and the bottom surface of the specimen by fixing the horizontal and vertical axes, respectively. A surface-to-surface frictionless hard contact was defined between the indenter and the sample in order to simulate their interaction. The indenter and the test sample were chosen as the master surface and the slave surface, respectively.

For the quantification of the constitutive parameters in each model, we use the nonlinear least-square algorithm in MATLAB and minimize the objective function in Eq. (9). Constraints were imposed based on the parameters in order to ensure a uniform sampling of the initial population. Multiple runs of the optimization algorithm as well as the second-order derivatives at the optimized point aimed at avoiding the identified parameter set that did not correspond to local minima. The identified parameter set obtained by minimizing the cost function was accepted as the optimal value.

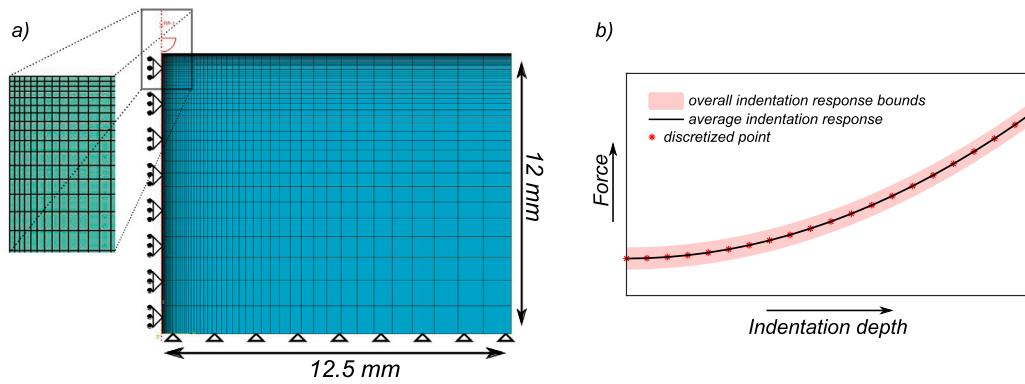$$f = \sqrt{\frac{\sum_{i=1}^{n}(F_{exp}(i) - F_{FE}(i))^2}{n}} \tag{9}$$

Fig. 2. (a) Axisymmetric finite element model used for the inverse parameter identification analysis. The red outline represents an analytical rigid surface to emulate the indenter. A refined mesh under the indenter, which gets coarser away from it; (b) discretization of the averaged experimental indentation response for the optimization algorithm.

In the above equation, *n* is the number of data points considered for each sample, following a spatial discretization of stretch ($n > 20$). F_{exp} and F_{FE} are the experimental and finite element model-derived force values at each point on the discretized indentation depth domain as shown in Fig. 2b.

2.5. Case study: known anisotropic hyperelastic material

Finally to assess the capability of the inverse finite element method a known, characterized anisotropic soft tissue was subjected to indentation. Bovine tracheal muscle tissue was chosen for the anisotropic material characterization, the detailed results of which are found in Ayyalasomayajula and Skallerud (2022). The mechanical response from the biaxial tension test is shown in Fig. 3. Briefly, the tissue was tested using a biaxial tension test rig to quantify its material response. Prior to material testing, the tissue sample was subjected to multi-photon microscopy (MPM) imaging to characterize its microstructure morphology. An anisotropic hyperelastic strain energy function proposed by Holzapfel et al. in Holzapfel et al. (2015) was used to characterize its constitutive behavior. The anisotropic strain energy function consisted of in total 5 (2 structural, 3 mechanical) unknown parameters as shown in Eq. (10). The two structural parameters can be estimated from MPM imaging, whereas the three mechanical parameters were estimated from the material's stress–strain response. The entire methodology and postprocessing are described in Ayyalasomayajula and Skallerud (2022).

$$\Psi^{ANI} = \frac{c}{2}(I_1 - 3) + \frac{k_1}{2k_2}[e^{k_2(tr(C\gamma_i I + (1-2\gamma_i)(M_i \otimes M_i))-1)^2} - 1] \quad (10)$$

where c, k_1, and k_2 are material constants. γ_i and M_i are fiber morphology parameters. The anisotropic response of the material is shown in Fig. 3.

3. Results

3.1. Indentation response

Figs. 4 and 5 show Force (P) vs indentation depth (d) curves obtained in macro-indentation experiments for all materials using a spherical indenter. All the estimated elastic moduli and their standard deviations are reported in Table 1.

3.1.1. Agarose phantoms

In order to verify the indentation test setup, a first set of tests was conducted on agarose phantom samples produced with a known range of elastic modulus. Three different agarose concentrations were used to produce the following elastic moduli: 10 kPa, 36 kPa, and 64 kPa. The average of 5 indentation tests along with the bounds is presented in Fig. 4 a–c. It can be seen that the range of estimated value of linear elastic moduli from the indentation tests was within a consistent limit of the theoretical value.
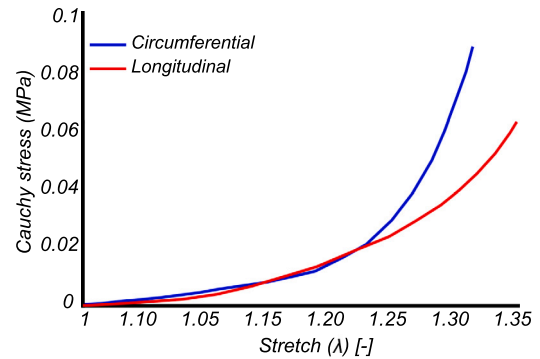

Fig. 3. Anisotropic stress–strain response of the bovine trachealis muscle obtained from biaxial tension testing.

3.1.2. Bovine liver

A total of 15 liver samples underwent the indentation test, obtained from 3 cows (five for each cow). The size of the samples selected for investigation was about 7.5 cm³. A total of 93 points were tested from 15 samples. The result from the indentation testing showed a consistent response with an elastic modulus of 3.41 ± 0.72 kPa.

3.2. Bovine lymph nodes

A total of 8 lymph nodes obtained from 3 cows were tested. Both slices for each lymph node with the largest cross-sectional area underwent the indentation test. A total of 84 points were tested from the 8 lymph nodes. As the lymph nodes were sliced through their central plane along the major axis of the ellipsoid, the thickness of the samples was not uniform. After conducting a pilot study, it was concluded that within the middle region, this does not affect the indentation response of the tissue. It is to be noted that embedding the samples within an agarose phantom could be better. However, the effect of the background material's stiffness to strain ratio and modulus ratio (ratio of Young's modulus of lymph node to that of the background material) is unknown. The size of the samples selected for investigation ranged from 12 mm to 23 mm (17.3 ± 3.8) along the longer axis and 8 mm to 16 mm (12.6 ± 2.9) along the short axis. The thickness of the nodes at their maximum inflection point was measured in the range of 9 mm to 14 mm (11.2 ± 3.1). The result of the indentation test showed that there was a significant difference ($p-value < 0.05$) between the Young's modulus of the bovine liver tissue (3.41 ± 0.48 kPa) compared to lymph nodes (21.78 ± 5.41 kPa). Unlike the liver tissue, the estimated elastic modulus within the lymph nodes varied from node to node with a low of 15.43 kPa and a high of 34.72 kPa. Within the peripheral and central regions of the lymph nodes, there was no significant difference
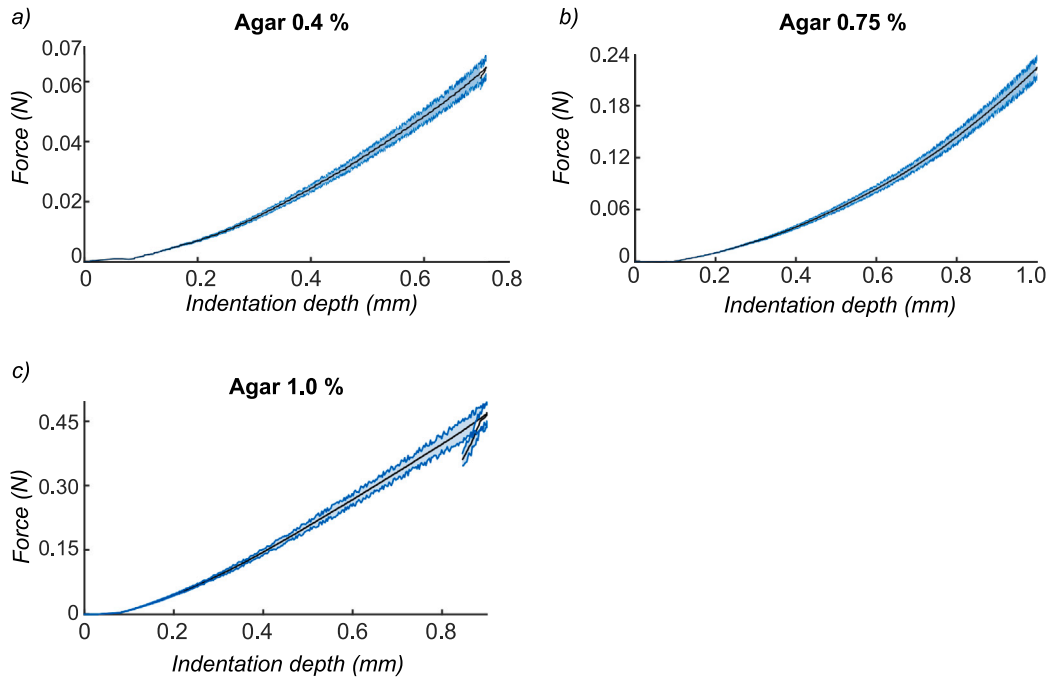
a) **Agar 0.4 %**

b) **Agar 0.75 %**

c) **Agar 1.0 %**

Fig. 4. (a–c) Indentation response for agarose phantoms.

Table 1
Average elastic moduli computed for agarose phantoms and liver samples for $\frac{d}{r} = 0.5$.

Material	Sample	Elastic modulus - indentation (E, kPa)	Elastic modulus - literature (E, kPa)
Agarose phantom	0.4%	10.7 ± 2.2	9.3 ± 1.8
	0.7%	36.3 ± 3.4	34.2 ± 1.4 (Barrangou et al., 2006)
	1.0%	71.2 ± 5.8	64.4 ± 2.7
Liver	1	2.87 ± 0.95	
	2	3.72 ± 0.61	3.8 ± 2.1 (Levental et al., 2010; Ahn et al., 2009; Barnes et al., 2007)
	3	3.96 ± 0.38	
	avg	3.41	
	std	0.48	
Lymph nodes	1	24.51 ± 1.59	
	2	22.87 ± 1.14	
	3	17.35 ± 2.67	
	4	21.64 ± 1.35	25.39 ± 6.14 (Yuen et al., 2011)
	5	30.81 ± 1.18	
	6	20.43 ± 1.55	
	7	19.61 ± 1.58	
	8	21.34 ± 1.76	
	avg	21.78	
	std	5.41	

($p > 0.05$) in the estimated elastic modulus (to comment on whether one region is stiffer than the other).

3.3. Inverse FE analysis

Finite element analysis was employed to inversely extract material parameters for an isotropic homogeneous material based on their recorded mechanical response from indentation tests.

3.3.1. Indentation depth to indenter radius ratio $\frac{d}{r} = 0.5$

Given the non-linear nature of the mechanical response, the initial loading region is explored first, up to an indentation ratio of 0.5.

The mean measured force–displacement curves for agarose phantoms, liver, and lymph nodes along with their corresponding best-fit material models are presented Fig. 6. Within the initial loading regime, it can be seen that the linear elastic and neo-Hookean model matched well to the experimentally obtained force–displacement curve with the least overall error. Yeoh hyperelastic model produced the least compatible fit of the explored hyperelastic material models. In general, the material constants corresponding to exponential terms were found to be highly variable and less significant. Table 2 shows the identified material parameters for all the models along with their 95% confidence intervals for the indentation depth ratio of $\frac{d}{r} = 0.5$. Although an acceptable fit was observed, the parameters for the Yeoh hyperelastic material model showed a large degree of uncertainty.

3.3.2. Indentation depth to indenter radius ratio $\frac{d}{r} = 1.5$

At greater indentation depths, geometric and material non-linearities become more apparent, which are not captured in the analytical solution. In this regard, the mean experimental data and the corresponding best-fit model response for liver and lymph nodes are shown in Fig. 7. An excellent fit was observed in both cases for the neo-Hookean model with a min r-square of 0.92. On the contrary, the linear elastic model deteriorated in terms of comparison to the experimental curve. Though non-linear effects were involved, Mooney–Rivlin and Yeoh hyperelasticity models did not successfully reproduce the experimental force–displacement curves with a mean R-square value of 0.86 and 0.85 respectively for the liver and 0.89 and 0.86 for lymph nodes respectively. However, the first-order Ogden model provided the best fit with an R-square of 0.96. Table 3 shows the identified material parameters for all the models along with their 95% confidence intervals for the indentation depth ratio of $\frac{d}{r} = 1.5$.

3.4. Case study: Anisotropic material ($\frac{d}{r} = 2$)

Bovine tracheal muscle tissue was characterized with an anisotropic hyperelastic material model as detailed in Eq. (10). The material anisotropy within the strain energy function was defined by 3 mechanical and 2 structural parameters. The two structural parameters were identified from thorough MPM investigations. The model was able to predict the mechanical parameters through an iterative process, while
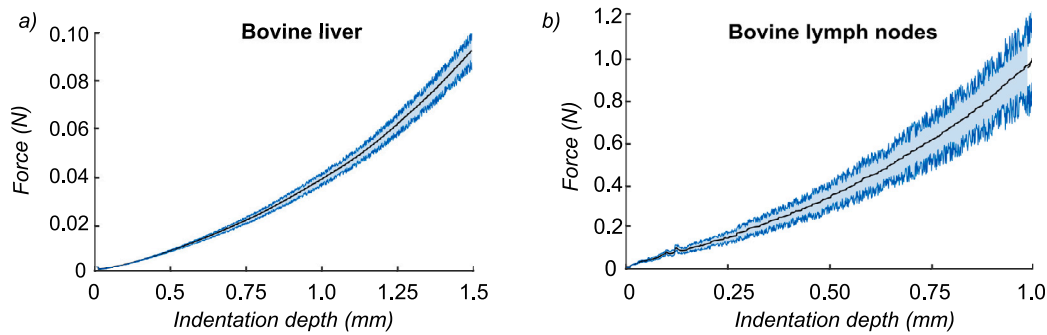
Fig. 5. Aggregate indentation response of (a) bovine liver tissue samples; (b) bovine lymph node samples.
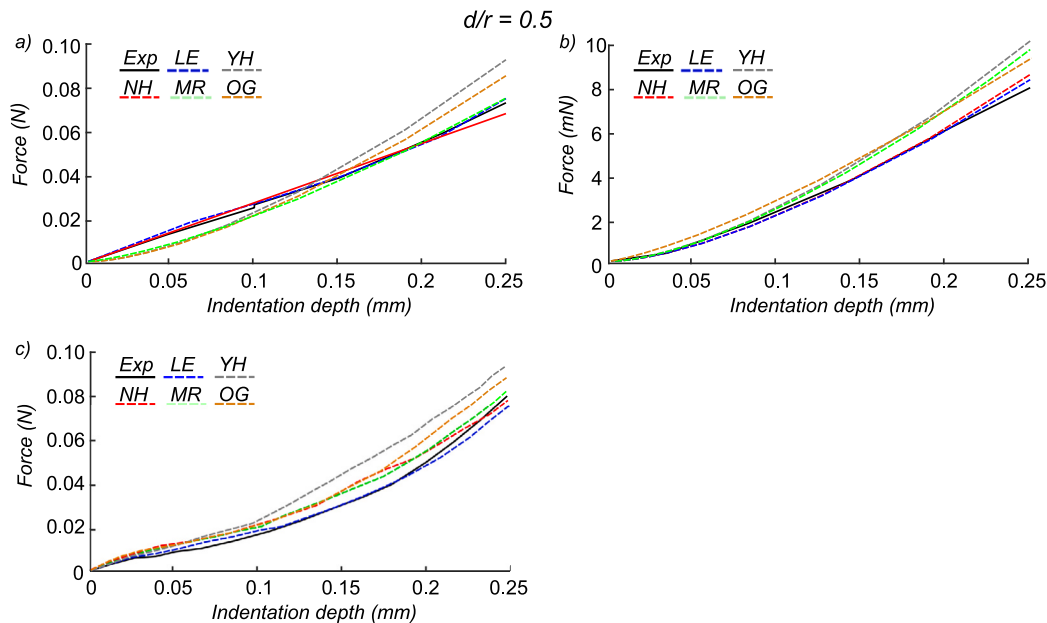

Fig. 6. Comparison between the average experimental data and best-fit modeling results for an indentation depth ratio of $\frac{d}{r} = 0.5$; (a) agar 1%; (b) bovine liver; (c) bovine lymph nodes. Exp — experimental curve, LE — linear elastic, NH — NeoHookean, MR — Mooney Rivlin, YH — Yeoh hyperelastic, OG — Ogden hyperelastic.

the structural parameters were obtained from second harmonic generation microscopy imaging (Ayyalasomayajula and Skallerud, 2022). The parameter identification was done through an iterative process, with the isotropic parameter (c) first identified within $\frac{d}{r} \leq 0.10$. Using that information, the anisotropic parameter set (k_1 and k_2) was identified on the whole curve. The identified optimal parameter set had an error of less than 10%. The parameter set identified from the experimental investigations and the iteratively obtained mechanical parameter set from inverse finite element simulations are shown in Table 4. It is worth noting that boundary constraints were imposed on the parameters which could have simplified the identification. On the other hand, no convergence was achieved with all the 5 parameters kept open for inverse identification. Fig. 8 shows the anisotropic material response recorded on a biaxial tension setup and its indentation response along with the two sets of identified material parameters.

4. Discussion

In this study, with the aim of providing a quantitative assessment of agarose hydrogel phantoms, bovine liver, and bovine lymph nodes' stiffness, an instrumented indentation examination with a spherical indenter of 0.5 mm radius was performed. The elastic modulus of the liver has been studied in some detail via indentation (Levental et al., 2010; Ahn et al., 2009; Barnes et al., 2007). In the case of agarose hydrogel phantoms, there has been no quantitative study to determine the shear

modulus of the phantoms for varying amounts of agarose concentration (Type I-A, low EEO, Agarose A0169, Sigma-Aldrich). In this case, the study provides the operating range of agarose phantom's shear modulus for 0.4%, 0.7%, and 1% w/v concentrations, which could be used in ultrasound shear wave imaging studies. Finally, only two studies report the elastic modulus of excised lymph nodes (Yuen et al., 2011; Miyaji et al., 1997). To provide a further quantitative assessment, bovine lymph nodes were also tested using instrumented indentation on sliced lymph node specimens for modulus determination.

The repeatability of the indentation system was found to be of a satisfactory level. Prior to this study, a separate repeatability study was conducted on 3 silicone samples with different stiffness. An intra-class correlation coefficient (ICC) of 0.99 was found, indicating a repeatability of 99%. For the liver samples, the indentation tests report an elastic modulus in the range of 0.6 kPa to 10 kPa (Barnes et al., 2007; Levental et al., 2010). The elastic modulus computed in this study from the experimental indentation curves is 3.41 ± 0.72 kPa is within the reported range of values.

In comparison to porcine lymph nodes (Yuen et al., 2011), the computed elastic modulus of 21.78 ± 5.41 kPa was softer in bovine lymph nodes and showed a larger degree of variation. The tests were only conducted on normal lymph nodes as they were excised from cows sacrificed for commercial consumption. Hence, as a general rule, the tested lymph nodes were assumed to not contain metastasis. During our sample preparation step, we found that some nodes appeared to
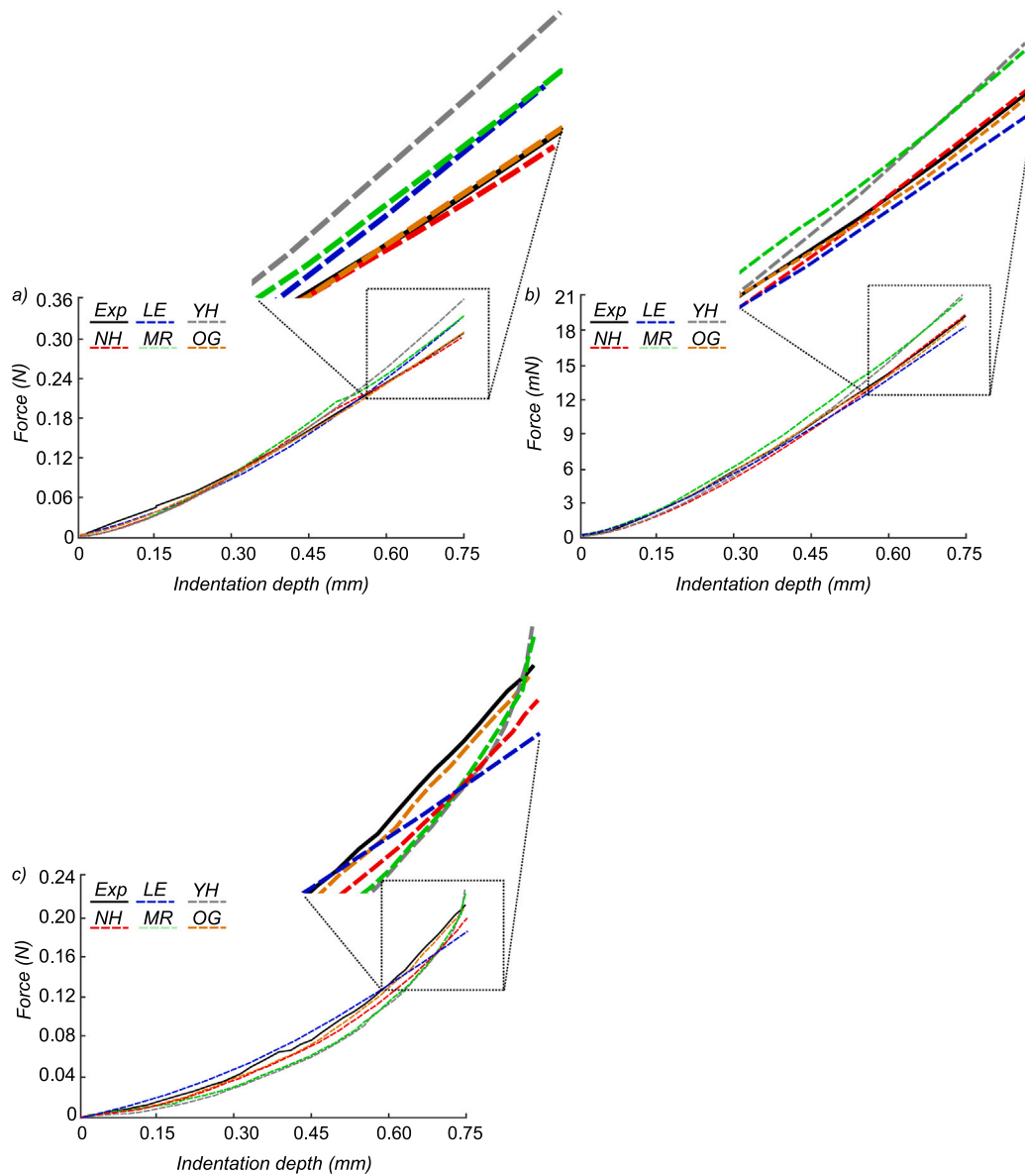
Fig. 7. Comparison between the average experimental data and best-fit modeling results for an indentation depth ratio of $\frac{d}{r} = 1.5$; (a) agar 1%; (b) bovine liver; (c) bovine lymph nodes. Exp — experimental curve, LE — linear elastic, NH — NeoHookean, MR — Mooney Rivlin, YH — Yeoh hyperelastic, OG — Ogden hyperelastic.
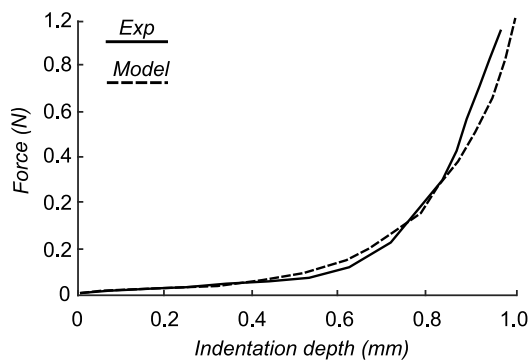

Fig. 8. Case study of a known anisotropic soft tissue: Comparison of indentation response to finite element model with inversely identified parameter set. The solid black line represents the indentation response of the anisotropic material, whose constitutive parameters were obtained from prior experimental investigations. The dashed line represents the best-fit indentation response, where mechanical parameters were identified iteratively while using the same structural parameters.

be congested and hemorrhagic as shown in Fig. 9. It was not certain whether this was caused by post-mortal changes or trauma, or it was an indication of abnormality or a disease. While comparing the data between the two visually distinct types of lymph nodes, no statistical significance was observed either in their anatomical measurements or their elasticity values ($p \geq 0.05$). As such, they were treated as healthy lymph nodes. Therefore, a comparison between healthy and abnormal lymph nodes could not be made in our current study. It would be interesting to explore the modulus changes in abnormal lymph nodes in future studies.

Sample thickness could be an important factor to consider along with indenter radius as the internal tissue could be heterogeneous. Slices of up to 2–3 mm in conjunction with an indenter of radius 0.2 mm would improve the resolution of testing along with comparability to elastography imaging data. Our trial suggested that thicker slices were of better quality for the indentation setup used in our study compared to thinner slices.

The estimated material parameters varied based on the analyzed $\frac{d}{r}$ ratio. For low $\frac{d}{r} < 0.5$, the analytical solution of the indentation

Fig. 9. Lymph nodes extracted from the cervical region of the cow, some of which show blackened texture. No statistical difference was recorded between the two in terms of gross anatomy or elasticity.

Table 2

Modeling accuracy of the force response during liver and lymph node indentation using different material models for an indentation depth ratio of $\frac{d}{r} = 0.5$.

Material model	Parameter	Optimum value (kPa)	95% confidence interval	R-square
Liver				
Linear elastic	E	2.77	2.48–3.12	0.98
neo-Hookean	C_1	0.51	0.46–0.64	0.97
Mooney–Rivlin	C_1	0.31	0.25–0.42	0.91
	C_2	0.17	0.13–0.26	
Yeoh	C_1	0.42	0.39–0.78	
	C_2	0.03	0.008–0.13	0.87
	C_3	0.01	0.003–0.08	
Ogden	μ	1.42	0.97–1.81	
	α	−2.4	(−1.9)–(−2.7)	0.93
Lymph nodes				
Linear elastic	E	18.61	15.72–22.54	0.94
neo-Hookean	C_1	3.68	3.45–4.04	0.96
Mooney–Rivlin	C_1	3.25	2.96–3.38	0.92
	C_2	0.78	0.59–0.85	
Yeoh	C_1	3.98	3.40–4.77	
	C_2	0.01	0.004–0.27	0.86
	C_3	0.006	0.0008–0.11	
Ogden	μ	5.14	4.35–8.28	
	α	−1.8	(−1.6)–(−2.7)	0.90

Table 3

Modeling accuracy of the force response during liver and lymph node indentation using different material models for an indentation depth ratio of $\frac{d}{r} = 1.5$.

Material model	Parameter	Optimum value (kPa)	95% confidence interval	R-square
Liver				
Linear elastic	E	3.27	3.08–3.51	0.89
neo-Hookean	C_1	0.63	0.52–0.75	0.92
Mooney–Rivlin	C_1	0.37	0.31–0.46	0.86
	C_2	0.18	0.13–0.28	
Yeoh	C_1	0.58	0.51–0.70	
	C_2	0.01	0.008–0.08	0.85
	C_3	0.003	0.0005–0.01	
Ogden	μ	1.42	0.97–1.81	
	α	−3.3	(−2.8)–(−3.7)	0.96
Lymph nodes				
Linear elastic	E	23.41	21.72–28.54	0.90
neo-Hookean	C_1	3.68	3.45–4.04	0.94
Mooney–Rivlin	C_1	3.25	2.96–3.38	0.89
	C_2	0.78	0.59–0.85	
Yeoh	C_1	3.98	3.40–4.77	
	C_2	0.01	0.004–0.27	0.86
	C_3	0.006	0.0008–0.11	
Ogden	μ	7.14	5.35–9.88	
	α	−3.7	(−3.1)–(−4.5)	0.98

Table 4

Material parameters of the anisotropic material model identified from biaxial tension test results and from the inverse fe model. Keep note of the constraints on the structural parameters, which are unchanged.

Parameter identification	Mechanical parameters			Structural parameters	
	c (kPa)	k_1 (kPa)	k_2 (kPa)	θ (M)	γ
Biaxial tension	1.8	1.1	4.2	76.4	1.36
Inverse FE	2.3	0.8	4.4	76.4	1.36

test overestimated the apparent elastic modulus compared to inverse FE analysis conducted on the loading part of the curve. Contrarily, the initial shear modulus computed with the FE model yielded a better estimate of the material's known elastic modulus. For $\frac{d}{r} > 0.5$, the estimated elastic modulus increased with increasing indentation depth within both the analytical and inverse FE solutions as seen in Table 3. Therefore, the inverse FE solution appears to be an accurate representation of the material's elastic modulus in the low-loading regime for ultra-soft biomaterials.

Linear elasticity is assumed often while estimating the elastic modulus from macro-indentation testing. It is interesting to note that from Tables 1–3, the identified elastic modulus from indentation for the liver (3.41 ± 0.48) and lymph nodes (21.78 ± 5.41) is closer to the linear elastic modulus inversely identified at $\frac{d}{r} = 1.5$. However, it can be seen from Figs. 6 and 7 that linear elastic models are not often the best-fit. This could imply that inverse fe identification of the material model parameters, even in the case of isotropic hyperelasticity is better than the use of macro-idantation's analytical solution. Mechanical testing of ultra-soft biomaterials provides a formidable challenge, particularly in uniaxial tension testing, which is often regarded as a gold standard for measuring elastic properties (Miller, 2005). However,

through this study, we also demonstrate that isotropic hyperelastic material properties of the tissues can be identified using a rapid inverse finite element analysis procedure. As seen from Fig. 6, for low $\frac{d}{r}$, the linear elastic material model makes the best estimate of the mechanical behavior, followed closely by the neo-Hookean hyperelastic model. We demonstrate that Mooney–Rivlin and Yeoh's hyperelastic models do not accurately represent the mechanical behavior of the tested materials.

For a high $\frac{d}{r}$ of 1.5, where non-linearity manifests noticeably, the first-order Ogden model makes the best estimation of the material's mechanical behavior. The results of this study showed that uniqueness can be ensured for models with up to two unknown material parameters. Although, the Yeoh hyperelastic model with 3 material
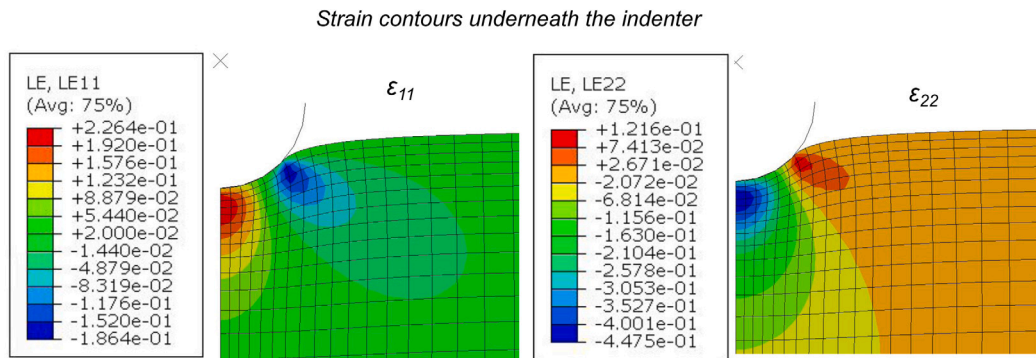
Strain contours underneath the indenter

Fig. 10. Logarithmic strain distribution in the x and y directions obtained by FEM simulation of the spherical indentation response of a hydrogel. The presence of tensile deformations is noted.

parameters compared relatively well to the experimental solution, it almost reduced to a neo-Hookean model with the two exponential parameters being identified close to zero. It is also to be noted that the Ogden model reduces to a neo-Hookean model for $\alpha = -2$. The identified value of α for larger indentation depths (-3.3) deviated significantly from this value.

Fig. 10 shows the principle strain contours under the indenter. Firstly, it can be seen that neither serious penetration nor zero-energy mode occurred in the simulation. Secondly, there are regions near the indenter in which the stress state is positive despite the major volume of material beneath the indenter being subjected to compressive stresses, which are actually larger than tensile ones. Lin et al. (2009) proposed indentation force-depth relations for several hyperelastic models assuming compressive stress states and validating them via finite element simulations. However, the level to which the tensile contribution to the overall indentation response can be neglected is unknown. Further, this can be significant in larger indentation depth ratios where adhesion also plays an important role in determining the elastic modulus.

Finally to assess the capability of the inverse finite element method a known, characterized anisotropic soft tissue was subjected to indentation. The anisotropic material was first tested using a biaxial tension test rig, with its collagen microstructure quantified using second harmonic generation imaging. An anisotropic strain energy function with 5 (2 structural, 3 mechanical) unknown parameters were used to reproduce the material's anisotropic response. Later, the same sample was tested via macro-indentation and an inverse analysis of its response was performed. The FE model was able to predict the mechanical parameters through an iterative process, assuming that the structural parameters were known as seen in Table 4 and Fig. 8. However, this is a special case of an anisotropic material model, where structural parameters could be derived from multi-photon microscopy investigations. For purely phenomenological models, the same approach would not be viable. Secondly, it is to be noted that the tissue was characterized by biaxial tension, whereas in indentation, the stress–strain state is essentially compression. Many researchers report the insignificant role of collagen fibers, which give rise to the high tensile stiffness and material anisotropy (Hariton et al., 2007). Therefore, the anisotropic material parameter identification done here via indentation must be verified with more data points.

5. Conclusion

In summary, this study investigates the elasticity of agarose hydrogel phantoms, bovine liver, and bovine lymph nodes via instrumented indentation testing. The choice of a 0.5 mm radius spherical indenter was well suited to test the samples at multiple points without any significant interference. This information could be used to compare and validate elasticity maps measured from ultrasound elastography. Further, we have evaluated four widely used hyperelastic models, i.e., neoHookean, Mooney–Rivlin, Yeoh model, and Ogden hyperelastic model based on inverse finite element analysis. Such a method is applicable when the indentation depth is comparable to the indenter radius. Only one or two material parameters are involved in the present inverse problems. Even though Yeoh model has three parameters, it is reduced to an almost neo-Hookean model. When more mechanical parameters are involved, the posed problem will be more complicated and the inverse procedure may not only suffer from the stability issue but also with existence and uniqueness issues. The macro indentation data overestimated the elastic modulus as compared to the inverse FE models for small strain deformations (low $\frac{d}{r}$ values). Further, pure elastic behavior can be assumed without errors to analyze the indentation data at low $\frac{d}{r}$ range. A case study on a known anisotropic material is presented, which revealed that full-scale anisotropic parameter identification is not viable based on indentation testing alone. It can be coupled however with a detailed investigation of the microstructure followed by a split inverse identification.

CRediT authorship contribution statement

Venkat Ayyalasomayajula: Writing – review & editing, Writing – original draft, Visualization, Validation, Methodology, Investigation, Formal analysis, Data curation, Conceptualization. **Øyvind Ervik:** Writing – review & editing, Resources, Methodology, Investigation, Conceptualization. **Hanne Sorger:** Writing – review & editing, Supervision, Resources, Project administration, Funding acquisition, Conceptualization. **Bjørn Skallerud:** Writing – review & editing, Supervision, Software, Resources, Project administration, Funding acquisition, Conceptualization.

Declaration of competing interest

The authors certify that they have NO affiliations with or involvement in any organization or entity with any financial interest (such as honoraria; educational grants; participation in speakers' bureaus; membership, employment, consultancies, stock ownership, or other equity interest; and expert testimony or patent-licensing arrangements), or non-financial interest (such as personal or professional relationships, affiliations, knowledge or beliefs) in the subject mater or materials discussed in this manuscript.

Data availability

Data will be made available on request.

References

Abushagur, A.A., Arsad, N., Ibne Reaz, M., Ashrif, A., Bakar, A., 2014. Advances in bio-tactile sensors for minimally invasive surgery using the fibre Bragg grating force sensor technique: A survey. Sensors 14 (4), 6633–6665.

Ahn, B.-M., Kim, Y.-J., Shin, J.H., Kim, J., 2009. Biomechanical characterization with inverse FE model parameter estimation: Macro and micro applications. Trans. Korean Soc. Mech. Eng. A 33 (11), 1202–1208.

Ayyalasomayajula, V., Skallerud, B., 2022. Microstructure and mechanics of the bovine trachea: Layer specific investigations through SHG imaging and biaxial testing. J. Mech. Behav. Biomed. Mater. 134, 105371.

Baatenburg de Jong, R., Rongen, R., Lameris, J., Harthoorn, M., Verwoerd, C., Knegt, P., 1989. Metastatic neck disease. Palpation vs ultrasound examination. Arch. Otolaryngol. Head Neck Surg. 115 (6), 689–690.

Barnes, S.L., Lyshchik, A., Washington, M.K., Gore, J.C., Miga, M.I., 2007. Development of a mechanical testing assay for fibrotic murine liver. Med. Phys. 34 (11), 4439–4450.

Barr, R.G., 2018. Shear wave liver elastography. Abdom. Radiol. 43, 800–807.

Barrangou, L.M., Daubert, C.R., Foegeding, E.A., 2006. Textural properties of agarose gels. I. Rheological and fracture properties. Food Hydrocolloids 20 (2–3), 184–195.

Bercoff, J., Tanter, M., Fink, M., 2004. Supersonic shear imaging: a new technique for soft tissue elasticity mapping. IEEE Trans. Ultrason. Ferroelectr. Freq. Control 51 (4), 396–409.

Brunon, A., Bruyere-Garnier, K., Coret, M., 2010. Mechanical characterization of liver capsule through uniaxial quasi-static tensile tests until failure. J. Biomech. 43 (11), 2221–2227.

Chai, C.-K., Akyildiz, A.C., Speelman, L., Gijsen, F.J., Oomens, C.W., van Sambeek, M.R., van der Lugt, A., Baaijens, F.P., 2013. Local axial compressive mechanical properties of human carotid atherosclerotic plaques—characterisation by indentation test and inverse finite element analysis. J. Biomech. 46 (10), 1759–1766.

Chen, Y., Qiu, S., He, Z., Yan, F., Li, R., Feng, Y., 2021. Comparative analysis of indentation and magnetic resonance elastography for measuring viscoelastic properties. Acta Mech. Sin. 37, 527–536.

Chui, C., Kobayashi, E., Chen, X., Hisada, T., Sakuma, I., 2004. Combined compression and elongation experiments and non-linear modelling of liver tissue for surgical simulation. Med. Biol. Eng. Comput. 42, 787–798.

Das, S., Skobe, M., 2008. Lymphatic vessel activation in cancer. Ann. New York Acad. Sci. 1131 (1), 235–241.

DePeña, C.A., Van Tassel, P., Lee, Y.-Y., 1990. Lymphoma of the head and neck.. Radiol. Clin. North Am. 28 (4), 723–743.

Feng, Y., Lee, C.-H., Sun, L., Ji, S., Zhao, X., 2017. Characterizing white matter tissue in large strain via asymmetric indentation and inverse finite element modeling. J. Mech. Behav. Biomed. Mater. 65, 490–501.

Ferraioli, G., Parekh, P., Levitov, A.B., Filice, C., 2014. Shear wave elastography for evaluation of liver fibrosis. J. Ultrasound Med. 33 (2), 197–203.

Franchi-Abella, S., Elie, C., Correas, J.-M., 2013. Ultrasound elastography: advantages, limitations and artefacts of the different techniques from a study on a phantom. Diagn. Interv. Imaging 94 (5), 497–501.

Fung, Y.-c., 2013. Biomechanics: Mechanical Properties of Living Tissues. Springer Science & Business Media.

Gao, Z., Lister, K., Desai, J.P., 2010. Constitutive modeling of liver tissue: experiment and theory. Ann. Biomed. Eng. 38 (2), 505–516.

Giannakopoulos, A., Triantafyllou, A., 2007. Spherical indentation of incompressible rubber-like materials. J. Mech. Phys. Solids 55 (6), 1196–1211.

Hamhaber, U., Grieshaber, F., Nagel, J., Klose, U., 2003. Comparison of quantitative shear wave MR-elastography with mechanical compression tests. Magn. Reson. Med.: Off. J. Int. Soc. Magn. Reson. Med. 49 (1), 71–77.

Han, L., Noble, J.A., Burcher, M., 2003. A novel ultrasound indentation system for measuring biomechanical properties of in vivo soft tissue. Ultrasound Med. Biol. 29 (6), 813–823.

Hariton, I., Debotton, G., Gasser, T.C., Holzapfel, G.A., 2007. Stress-driven collagen fiber remodeling in arterial walls. Biomech. Model. Mechanobiol. 6, 163–175.

Hay, J., 2009. Introduction to instrumented indentation testing. Exp. Tech. 33 (6), 66–72.

Holzapfel, G.A., Niestrawska, J.A., Ogden, R.W., Reinisch, A.J., Schriefl, A.J., 2015. Modelling non-symmetric collagen fibre dispersion in arterial walls. J. R. Soc. Interface 12 (106), 20150188.

Holzapfel, G.A., et al., 2001. Biomechanics of soft tissue. Handb. Mater. Behav. Models 3 (1), 1049–1063.

Hoodeshenas, S., Yin, M., Venkatesh, S.K., 2018. Magnetic resonance elastography of liver-current update. Top. Magn. Reson. Imaging: TMRI 27 (5), 319.

Hu, T., Desai, J.P., 2004. Characterization of soft-tissue material properties: large deformation analysis. In: International Symposium on Medical Simulation. Springer, pp. 28–37.

Huang, Y., Zheng, J., Zeng, J., Wang, X., Wu, T., Zheng, R., 2014. Normal liver stiffness in healthy adults assessed by real-time shear wave elastography and factors that influence this method. Ultrasound Med. Biol. 40 (11), 2549–2555.

Kiss, M.Z., Daniels, M.J., Varghese, T., 2009. Investigation of temperature-dependent viscoelastic properties of thermal lesions in ex vivo animal liver tissue. J. Biomech. 42 (8), 959–966.

Lee, H., Pharr, G.M., Nahm, S.H., 2003. Material property evaluation of hyper-elastic rubber by micro-indentation. In: Proceedings of the SEM Annual Conference and Exposition on Experimental and Applied Mechanics.

Levental, I., Levental, K., Klein, E., Assoian, R., Miller, R., Wells, R., Janmey, P., 2010. A simple indentation device for measuring micrometer-scale tissue stiffness. J. Phys.: Condens. Matter 22 (19), 194120.

Lin, D.C., Shreiber, D.I., Dimitriadis, E.K., Horkay, F., 2009. Spherical indentation of soft matter beyond the hertzian regime: numerical and experimental validation of hyperelastic models. Biomech. Model. Mechanobiol. 8, 345–358.

Markert, C.D., Guo, X., Skardal, A., Wang, Z., Bharadwaj, S., Zhang, Y., Bonin, K., Guthold, M., 2013. Characterizing the micro-scale elastic modulus of hydrogels for use in regenerative medicine. J. Mech. Behav. Biomed. Mater. 27, 115–127.

Masuzaki, R., Tateishi, R., Yoshida, H., Sato, T., Ohki, T., Goto, T., Yoshida, H., Sato, S., Sugioka, Y., Ikeda, H., et al., 2007. Assessing liver tumor stiffness by transient elastography. Hepatol. Int. 1 (3), 394–397.

Mattei, G., Ahluwalia, A., 2016. Sample, testing and analysis variables affecting liver mechanical properties: A review. Acta Biomater. 45, 60–71.

Mazza, E., Nava, A., Hahnloser, D., Jochum, W., Bajka, M., 2007. The mechanical response of human liver and its relation to histology: an in vivo study. Med. Image Anal. 11 (6), 663–672.

McIlvain, G., Ganji, E., Cooper, C., Killian, M.L., Ogunnaike, B.A., Johnson, C.L., 2019. Reliable preparation of agarose phantoms for use in quantitative magnetic resonance elastography. J. Mech. Behav. Biomed. Mater. 97, 65–73.

Melly, S.K., Liu, L., Liu, Y., Leng, J., 2021. A review on material models for isotropic hyperelasticity. Int. J. Mech. Syst. Dyn. 1 (1), 71–88.

Miller, K., 2005. Method of testing very soft biological tissues in compression. J. Biomech. 38 (1), 153–158.

Miyaji, K., Furuse, A., Nakajima, J., Kohno, T., Ohtsuka, T., Yagyu, K., Oka, T., Omata, S., 1997. The stiffness of lymph nodes containing lung carcinoma metastases: a new diagnostic parameter measured by a tactile sensor. Cancer: Interdiscip. Int. J. Am. Cancer Soc. 80 (10), 1920–1925.

Namani, R., Simha, N., 2009. Inverse finite element analysis of indentation tests to determine hyperelastic parameters of soft-tissue layers. J. Strain Anal. Eng. Des. 44 (5), 347–362.

Nava, A., Mazza, E., Furrer, M., Villiger, P., Reinhart, W., 2008. In vivo mechanical characterization of human liver. Med. Image Anal. 12 (2), 203–216.

Oudry, J., Chen, J., Glaser, K.J., Miette, V., Sandrin, L., Ehman, R.L., 2009. Cross-validation of magnetic resonance elastography and ultrasound-based transient elastography: A preliminary phantom study. J. Magn. Reson. Imaging: Off. J. Int. Soc. Magn. Reson. Med. 30 (5), 1145–1150.

Pan, Y., Zhan, Y., Ji, H., Niu, X., Zhong, Z., 2016. Can hyperelastic material parameters be uniquely determined from indentation experiments? RSC Adv. 6 (85), 81958–81964.

Postmus, P., Kerr, K., Oudkerk, M., Senan, S., Waller, D., Vansteenkiste, J., Escriu, C., Peters, S., 2017. Early and locally advanced non-small-cell lung cancer (NSCLC): ESMO clinical practice guidelines for diagnosis, treatment and follow-up. Ann. Oncol. 28, iv1–iv21.

Samani, A., Plewes, D., 2004. A method to measure the hyperelastic parameters of ex vivo breast tissue samples. Phys. Med. Biol. 49 (18), 4395.

Sangpradit, K., Liu, H., Dasgupta, P., Althoefer, K., Seneviratne, L.D., 2011. Finite-element modeling of soft tissue rolling indentation. IEEE Trans. Biomed. Eng. 58 (12), 3319–3327.

Shuman, D.J., Costa, A.L.d.M., Andrade, M.S., 2006. Calculating the elastic modulus from instrumented indentation reload curves. In: Cbecimat.

Smith, M., 2010. ABAQUS/Standard User's Manual, Version 6.10. Dassault Systèmes Simulia Corp, United States.

Tourasse, C., Dénier, J.F., Awada, A., Gratadour, A.-C., Nessah-Bousquet, K., Gay, J., 2012. Elastography in the assessment of sentinel lymph nodes prior to dissection. Eur. J. Radiol. 81 (11), 3154–3159.

Venkatesh, S.K., Yin, M., Ehman, R.L., 2013. Magnetic resonance elastography of liver: technique, analysis, and clinical applications. J. Magn. Reson. Imaging 37 (3), 544–555.

Vilmann, P., Clementsen, P.F., Colella, S., Siemsen, M., De Leyn, P., Dumonceau, J.-M., Herth, F.J., Larghi, A., Vazquez-Sequeiros, E., Hassan, C., et al., 2015. Combined endobronchial and esophageal endosonography for the diagnosis and staging of lung cancer: European society of gastrointestinal endoscopy (ESGE) guideline, in cooperation with the European respiratory society (ERS) and the European society of thoracic surgeons (ESTS). Endoscopy 47 (06), 545–559.

Yang, Y., Li, K., Sommer, G., Yung, K.-L., Holzapfel, G.A., 2020. Mechanical characterization of porcine liver properties for computational simulation of indentation on cancerous tissue. Math. Med. Biol.: J. IMA 37 (4), 469–490.

Yuen, Q.W.-H., Zheng, Y.-P., Huang, Y.-P., He, J.-F., Cheung, J.C.-W., Ying, M., 2011. In-vitro strain and modulus measurements in porcine cervical lymph nodes. Open Biomed. Eng. J. 5, 39.

Zisis, T., Zafiropoulou, V., Giannakopoulos, A., 2015. Evaluation of material properties of incompressible hyperelastic materials based on instrumented indentation of an equal-biaxial prestretched substrate. Int. J. Solids Struct. 64, 132–144.